Proceedings of the Twenty-second (2012) International Offshore and Polar Engineering Conference **www.isope.org**
Rhodes, Greece, June 17–22, 2012

ISBN 978-1-880653-94–4 (Set); ISSN 1098-6189 (Set)

SPH Modeling of Plunging Wave Breaking, Surf Zone Turbulence and Wave-Induced Currents

Christos V. Makris, Yannis N. Krestenitis
Department of Civil Engineering, Faculty of Engineering,
Aristotle University of Thessaloniki
AUTh Campus, Thessaloniki, Macedonia, Greece

Constantine D. Memos
School of Civil Engineering, National Technical University of Athens
Zografos, Athens, Attiki, Greece

ABSTRACT

Computational modeling aspects of weak plunging wave breaking, over a relatively mild sloping laboratory beach, were investigated in the present paper. Comparisons against latest elaborate experimental data were used to support the discussion. Smoothed Particle Hydrodynamics method was implemented as a numerical tool and the recently enhanced version of the academic 'open source' code SPHysics v.2 was ratified. Fine spatial resolution calibration was undertaken in an attempt to render effective a Sub-Particle Scale Smagorinsky-type turbulence closure that treats energy dissipation of eddy formations for the unresolved flow scales. Fine visual reproduction of the ragged free-surface flow deformation was supplemented with plausible results concerning classic wave dynamics characteristics, sophisticated turbulent surf-zone features and wave-induced currents.

KEY WORDS: SPH; plunging wave breaking; Smagorinsky; coherent turbulent structures; vorticity; undertow; Stokes drift

INTRODUCTION

Near-shore wave breaking, consequent turbulence transport and the resulting mean flows in the surf zone have always been and still remain major issues for engineers and scientists in their quest to comprehend, fully describe and predict the evolution of coastal processes. Particularly in the surf zone, the wave pattern goes through extremely abrupt changes and the emerging flow field becomes highly unstable and violent, especially during plunging-type wave breaking. Physical modeling of the latter over even, mild sloping, laboratory beach-type formations (e.g. Ting & Kirby, 1994) has set the grounds of profound insight on the matter, yet experimental efforts relate always to specific hydraulic and geometric laboratory conditions. Nowadays the use of conditionally flexible enhanced computational approaches is imperatively necessary. Thus rigorous validation of them discerns among modern coastal hydrodynamics research endeavours.

In this framework, Grilli et al. (2001) used a higher-order Boundary Element Method (BEM) to simulate a 3D overturning solitary wave, yet only in terms of free surface elevation. The respective velocity field was reproduced in Guyenne and Grilli (2003), though not including any vortical pattern representation. Biausser et al. (2003) developed a coupled BEM-Volume of Fluid (VOF) method to fully simulate the plunging breaking yet again not of wave trains but of a solitary wave. Reynolds-Averaged Navier-Stokes (RANS) velocity fields and kinetic energy contours under plunging breakers were presented by Bradford (2000), without description of the vorticity patterns of the flow. An exquisite numerical study was performed by Watanabe and Saeki (2002), in which the vorticity in the coherent large-scale eddy structures was investigated. Moreover spatial gradients in frequency spectra of kinetic energy and enstrophy were associated with Reynolds stress production, transport and dissipation at various turbulent mixing length scales. Mean velocity field, wave and turbulent kinetic energy in the surf zone were also evaluated. The study incorporated though an arduous mesh-based VOF technique. A similar thorough investigation was accomplished by Zhao et al. (2004) implementing too a VOF technique together with a Sub-Grid Scale (SGS) approximation. Iafratti (2009) implemented a strenuous Level Set technique for the complete simulation of a plunging breaker examining the 2-phase air-entrainment flow. Tian et al. (2010) used an eddy viscosity approach to model only the energy dissipation for 2D unsteady plunging breakers. Lubin et al. (2011) only recently employed a Large Eddy Simulation (LES) model to simulate the violent free surface deformations and the detailed velocity vector field under plungers, without further analysis on turbulent features of the flow. Following our precedent research efforts (Makris et al., 2009; 2010a; 2010b; 2011) on the subject, we pursued in the present paper the improvement of our earlier investigations by incorporating newer, more elaborate versions of mesh-free computational modeling. Smoothed Particle Hydrodynamics (SPH), thoroughly presented by Monaghan (2005), was employed based on refined resolution and calibrated against experimental data in order to validate the method's ability to predict the details of the entire wave breaking process. In recent literature, the results of SPH simulations albeit visually impressive (Gómez-Gesteira et al., 2010b; Dalrymple and Rogers, 2006) display lack of thorough affirmation concerning averaged or turbulent flow features. Shao and Ji (2006) brought forth a LES-like SPH approach by using a Sub-Particle Scale (SPS) turbulence closure model. They produced notable results yet only for free surface displacements and turbulent intensities. Khayyer et al. (2008) made use of a Corrected Incompressible SPH method to accurately represent the free surface warping. They persisted only on resolution refinement and tried to justify convergence of numerical results with experimental ones

based only on plunging jet topology. Phase-averaged velocity fields, wave-induced mean flows in the surf zone, coherent turbulent structures, characteristic vortical patterns and other turbulent features were generally overlooked. Therefore we revisited our previously published analysis and provided in the present paper refined SPH-SPS numerical simulations of monochromatic nonlinear waves breaking in a weakly plunging form on a plane and relatively mild impermeable slope, replenished with all the above elaborate flow features.

METHODOLOGY

In this section the numerical approach used is presented, together with the experimental configuration selected as basis for calibration tests.

SPH Numerical Modeling

SPH is a Lagrangian mesh-free method, incorporating integral interpolation smoothing functions for the Navier-Stokes equations. Its particle discretization technique allows the unhampered simulation of free-surface flows with severe deformations (Dalrymple and Rogers, 2006; Gómez-Gesteira et al., 2010b). The method's distinctive attribute is the analytic representation of any given function $A(\mathbf{r})$ (scalar or vectorial) and its derivatives at a specific point as an integral interpolation of it over the surrounding computational domain that finally reads in discrete notation as:

$$A(\mathbf{r}) = \int A(\mathbf{r}')W(\mathbf{r}-\mathbf{r}',h)\,d\mathbf{r}' \Rightarrow A(\mathbf{r}) = \sum_j A_j\left(m_j/\rho_j\right)W_j \qquad (1)$$

where h is the smoothing length, $\mathbf{r}$, $\mathbf{r}'$ the arbitrary particle point location and distance between particles respectively, $W(\mathbf{r},h)$ a distance varied weighting (bell-shaped) function called kernel (W_j in particle notation), m_j, ρ_j the mass and density of particle j respectively. Detailed review of the SPH method can be traced in Monaghan (2005). Vital conjectures of the implementation used here are presented in our previous work (Makris et al., 2009) and Gómez-Gesteira et al. (2010b).

SPHysics Model

In this framework we have long chosen to get involved with the robust academic 'open source' numerical code SPHysics. Following the reasoning in Makris et al. (2011) the recent series version 2 (Gómez-Gesteira et al., 2010a) was utilized. Extended calibration of older versions can be checked in Makris et al. (2010a; b) and consequent presently assumed numerical aspects can be found in Makris et al. (2011). Similar fine spatial resolutions were implemented in the present investigation, which was enriched with more quantitative results and discussion, shedding further light in the surf zone turbulent features.

SPS Turbulence Closure Model

Viscosity treatment was based on a SPS approach Gotoh et al. (2001) akin to LES-SGS models used in traditional mesh-based methods. It all added up to a turbulence closure model for the handling of the unresolved scales, below spatial discretization Δx. The SPS stress tensor was modelled on an eddy viscosity assumption (Boussinesq hypothesis) supported by an artificial compressibility concept through a Favre-type averaging technique for the calculated density. A standard non-dynamic Smagorinsky-type model was applied for the derivation of turbulent eddy viscosity, v_t:

$$v_t = \left[\min\left(C_s\Delta l\right)\right]^2\left|\tilde{\mathbf{S}}_{ij}\right| \qquad (2)$$

where the Smagorinsky coefficient C_s was kept constant throughout the computational field. Δl is the inter-particle spacing and $\mathbf{S}_{ij}$ is the SPS strain rate tensor, for which the following applies:

$$\left|\tilde{\mathbf{S}}_{ij}\right| = \left(2\tilde{\mathbf{S}}_{ij}\tilde{\mathbf{S}}_{ij}\right)^{1/2}, \tilde{\mathbf{S}}_{ij} = -\frac{1}{2}\left(\frac{\partial\tilde{\mathbf{u}}_i}{\partial x_j}+\frac{\partial\tilde{\mathbf{u}}_j}{\partial x_i}\right) \qquad (3)$$

where $\mathbf{u}$ is the velocity vector and the tilde symbol (~) denotes Favre-type averaging. In Gómez-Gesteira et al. (2010a) this section is covered thoroughly by a short overview on LES-SPS turbulence modeling for SPHysics. The model was also backed up by a Shepard density averaging filter to ensure physically plausible smoothness of the free surface during violent deformations like plunging jet formation, overturning and splash-up (Makris et al., 2009). In order for the SPS model to work properly, correct calibration of the spatial resolution in SPHysics v.2 model needed to be completed in the first place. Thus particle discretizaztion Δx should be equal or smaller than specified real flow length scales, e.g. integral turbulence ones, which could be modelled by SPH in reasonable simulation times. For the purposes of the present paper, those values were derived by us from experimental data available.

Experimental Data

The experimental data adopted for comparison against numerical simulation output were collected by the physical modeling effort of Stansby & Feng (2005) [SF05 hereafter] in a laboratory flume installation. Their investigation covered variously the weak plunging breaking of near-shore nonlinear waves and consequent turbulence transport under them. The configuration features of the experimental setup and its outcome, used as basis for our numerical wave flume simulations for SPHysics v.2 affirmation, were previously presented in Makris et al. (2009; 2010a,b). Extended report can be found in SF05.

Calibration Test Cases

Table 1. Discrete simulation test cases based on spatial resolution Δx and other calibration factors

Test Case	Δx (m)	Calibrated Factors	Test Case	Δx (m)	Calibrated Factors
1	0.02	Δx/h = 0.77	7	0.005	Δx/h = 0.77
2	0.02	Δx/h = 0.58	8	0.006	Δx/h = 0.77
3	0.015	Δx/h = 0.77	9	0.00592	Δx/h = 0.77
4	0.01	Δx/h = 0.77	10	0.00632	Δx/h = 0.77
5	0.01	Δx/h = 0.58	11	0.0061	Δx/h = 0.77
6	0.01	t_o= 121 sec Δx/h = 0.77	12	0.004	Δx/h = 0.77
			13	0.003	Δx/h = 0.77

Following the analysis in Makris et al. (2011), the test cases employed are based mostly on spatial resolution (Table 1). Note that in test case 6 a time-consuming recording effort, involving 50 wave periods, was attempted in order to track its influence on Fourier spectral analysis of the turbulent components of the velocity at specific gauges. Test cases 9 to 11 correspond to requisite spatial resolution that marginally suffuses the integral turbulence length scales computed in the incipient wave breaking region, where strong shear effects prevail. Cox et al. (1994) estimate that the above scales vary from 0.04 to 0.18 of the water depth, for the initial breaking region and the inner surf zone respectively. We derived those values to range from 5.92 to 6.32 mm and from 1.35 to 1.71 cm for the outer and the inner surf zone of the

SF05 experiment respectively. Finer resolution than the inner surf zone integral turbulence length scale was used for almost every simulation test case (except the first two cases).

RESULTS AND DISCUSSION

In the following, various SPHysics v.2 numerical results are presented, ranging from depictions of the breaking process and comparable wave characteristics to representations of sophisticated turbulent features.

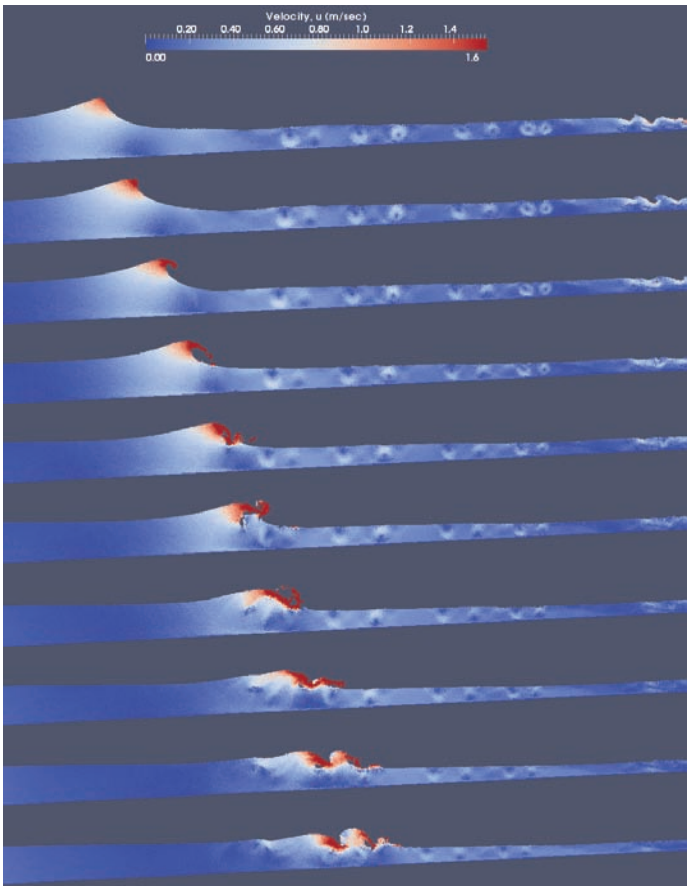

Fig. 1: Consecutive captured SPHysics output realistic depictions (with ParaView) of weak plunging wave breaking and consequent turbulent bore formation for fine particle resolution. Colour scale in respect to raw velocities.

Depiction of Near-Shore Plunging Wave Breaking

In Fig. 1 a streaming sequence of instantaneous SPHysics results depictions for fine particle resolution is portrayed. The time-step of projection was 0.1 sec. Brilliant qualitative agreement between numerical and experimental output was achieved, as the weak plunging incident reported in SF05 was exceptionally reproduced. The propagating surface roller gradually transformed into an oblique pointy bulge of water at the wave crest which was forced by excess in momentum to the formation of a protruding jet. Consequently the surface jet overturned and plunged into the forward trough impinging at the toe region of the roller. This constitutes the main mechanism of vorticity generation and enhancement due to turbulent production in plunging wave breaking. Subsequently a smaller rebound splash-up tongue was created which in turn flipped and plunged in front of the meanwhile formed turbulent bore. The latter propagated firmly creating a steep front which pushed the forward plash into the formation of a secondary free-surface bulge shoreward of the broken surface roller. A smaller plunging jet reappeared at the newly created bore front. Successive, sightly reproduced, cavities manifested themselves until the double water lump subsided and transformed into ripples at the swash zone. Colour scale in Fig. 1 refers to velocity magnitudes, whose values at the propagating crest of the breaking wave and the bore fronts reached a maximum of 1.6 times the theoretical shallow water celerity, $c_t=(g\cdot d)^{1/2}$. This value was slightly bigger compared to the experimentally measured wave speed, $1.32\cdot c_t$ (SF05). The latter was although surprisingly close to that found by Stive (1984) for spilling and not plunging breakers. Results of coarser resolution revealed a better match in terms of raw bore front velocities, yet finer spatial discretization invoked higher quality representation of the plunger. Another interesting feature in Fig. 1 is the representation of four couples of detached anti-clockwise large eddy formations that migrated leisurely towards the upcoming breaking wave until they blended with the turbulent motions there. They reappeared, regained a coherent shape and drifted very slowly offshore after the passing and reduction of the turbulent bore. In Fig. 2 the particle computational domain is represented in a vertical cross-section, for fine particle resolution (test 12). Past simulations (Makris et al., 2009; 2010a; 2010b) implemented nearly $2\cdot10^4$ particles (just like tests 1 and 2 in the present study), whereas tests 3 to 13 pertained from almost $5\cdot10^4$ to $2\cdot10^5$ ones. The run-up in the swash zone is clearly depicted (Fig. 2) and no further numerical treatment for the free surface coastal boundary is needed for that in the SPHysics model. The formerly excessive solid-water particle repulsion at the bed near the coastline margin (Makris et al., 2009; 2010a) was dealt with, through refinement of resolution. Nevertheless friction and boundary layer treatment is still poor in SPH simulations.

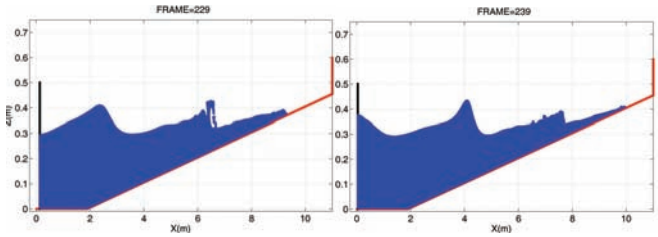

Fig. 2: SPHysics particle computational domain output frames (with Matlab) for weak plunging wave breaking. Axes are deformed.

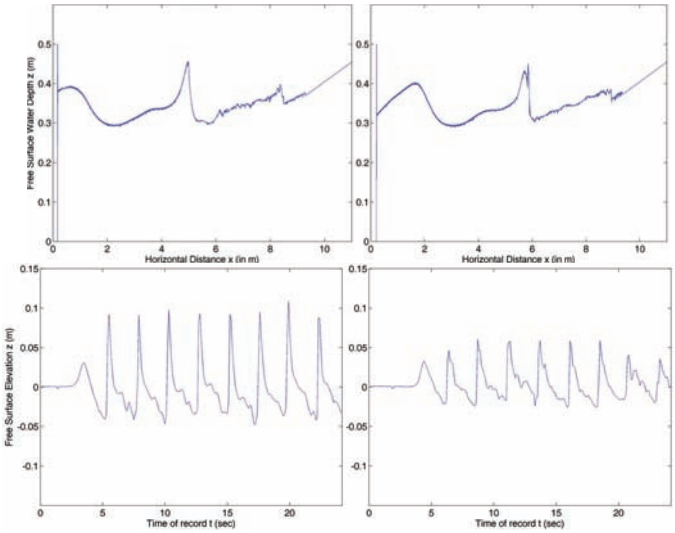

Fig. 3: SPHysics free-surface elevation snapshots [upper graphs] and time-series at specific gauges in the incipient breaking region (left) and the inner surf zone (right) [lower graphs].

Free-surface Elevation Patterns, Wave Height and Setup

Simulated free-surface elevation patterns for test 13 are presented in Fig. 3. The upper graphs reveal a reasonable depiction of the nonlinear monochromatic wave. The smoother than before (Makris et al., 2009) free-surface elevation pattern corresponds to the propagation region whereas the rough part defines the surf zone. In the lower graphs of Fig. 3 nonlinear undular forms of the free-surface elevation time-series are shown at certain gauges. Stability in pattern, strikingly similar to that reported in Zhao et al. (2004) for plunging breakers, is reached within a few simulated wave periods.

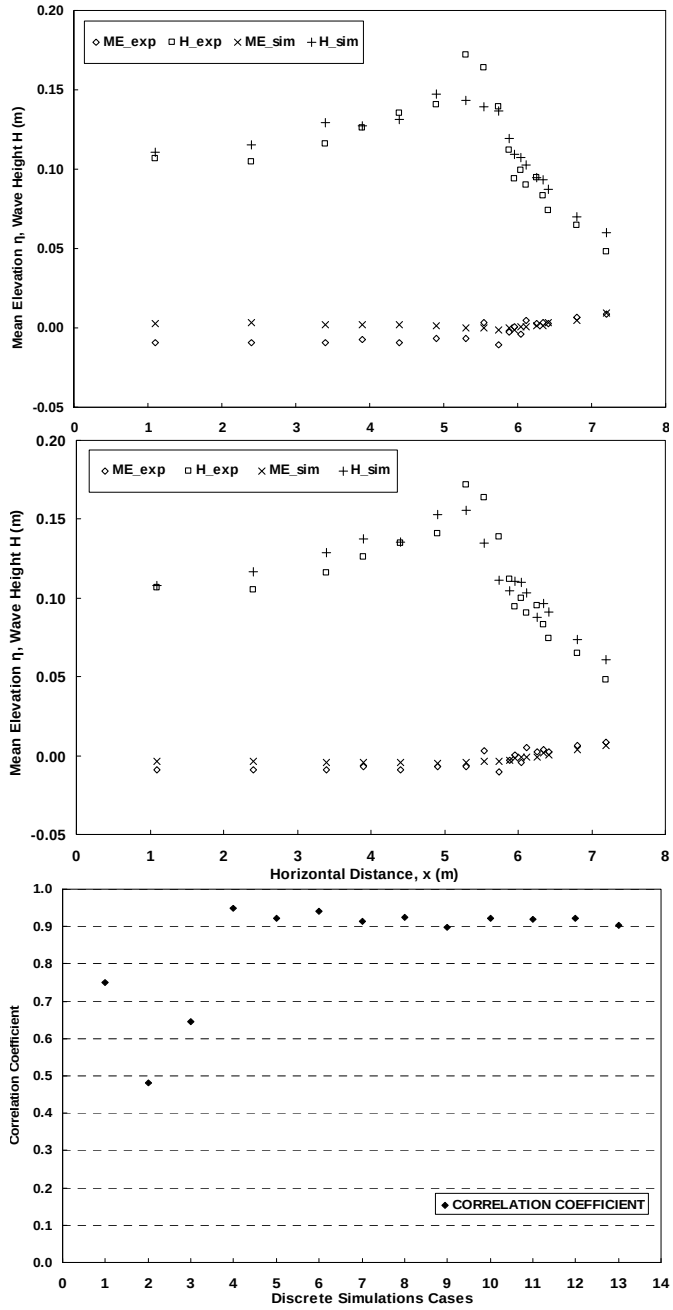

Fig. 4: Wave height 'H' and mean free-surface elevation 'ME' distribution comparisons between experiments (exp) and simulation (sim) test 4 [upper graph] & test 13 [mid graph]. Pearson correlation coefficients of discrete simulations between experimental and simulation output for wave height distributions [lower graph].

In Fig.4 comparisons of wave heights and setup for lower (upper graph) and higher (mid graph) resolution are shown. Agreement was plausible for all cases with $\Delta x \leq 1$ cm. Correlation coefficients (lower graph, Fig. 4) of the order of 0.9 and higher for wave height distributions throughout the whole computational domain corroborated the latter. Those values were obtained with the use of the classic Pearson formula:

$$CORR(X,Y) = \left(\frac{\sum_{k=1}^{n} \left(X_k - \overline{X}\right) \cdot \left(Y_k - \overline{Y}\right)}{\sum_{k=1}^{n} \left(X_k - \overline{X}\right)^2 \cdot \sum_{k=1}^{n} \left(Y_k - \overline{Y}\right)^2} \right) \quad (4)$$

where X and Y are experimentally and numerically derived values respectively of arbitrary flow features, n is the magnitude of the samples, k is the sum index and the macron symbol ($\overline{\ }$) denotes sample means. However, finer spatial resolution appeared to give better results for wave heights in the formerly (Makris et al. 2009; 2010a) problematic for SPH-SPS simulations incipient breaking region, where strong shear dominated. In other regions different resolution choices may have yielded better results, based on optimum dimensionless spacing $\Delta x/h$ values. Please note that the higher the $\Delta x/h$ factor became (small smoothing length), the more instabilities in the flow field occurred and the numerical benefits from SPH concept were enfeebled. On the other, hand low values of $\Delta x/h$ (large smoothing length) led to excessive smoothing of the flow properties and gave rise to spurious dissipative behavior of the SPH model. Nonetheless the wave setup (not setdown) was gradually impressively predicted as resolution got refined. In Fig. 5 surf zone crest and trough envelopes comparisons are presented for a fine resolution test case, with acceptable overlapping.

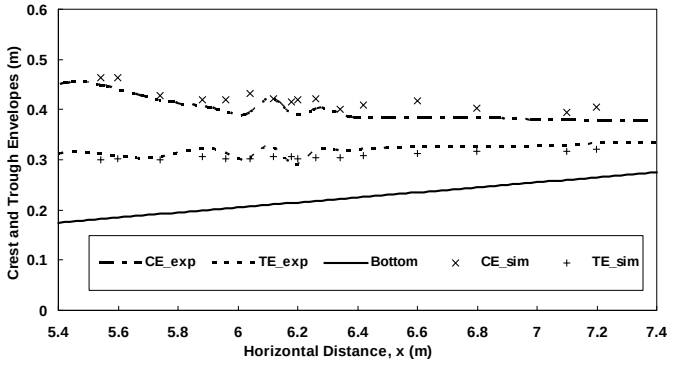

Fig. 5: Crest and trough envelopes, 'CE' and 'TE', between experimental (exp) and simulation (sim) output for test 12.

Phase-averaged Free-surface Elevation and Depth-averaged Velocities

The heuristic approach to analyze the turbulence flow field structure under breaking waves, rendered by Nadaoka et al. (1989) was used to define the ensemble-averaged values of e.g. the depth-averaged velocity **U** by calculating the phase-averaged values of it, <**U**> as:

$$\left\langle \mathbf{U}(\mathbf{x},\zeta t) \right\rangle = \frac{1}{N} \sum_{i=0}^{N-1} \mathbf{U}\left(\mathbf{x},\zeta\left(t+iT\right)\right) \quad (5)$$

where <·> is the phase-average operator, N is the maximum sample number similar to the wave cycles ($N \geq 10$), T is the wave period, ζ is the angular frequency, **x** is the position vector and t is the time interval of computations. The same formula (Eq. 5) was applied also for the free-surface elevation η.

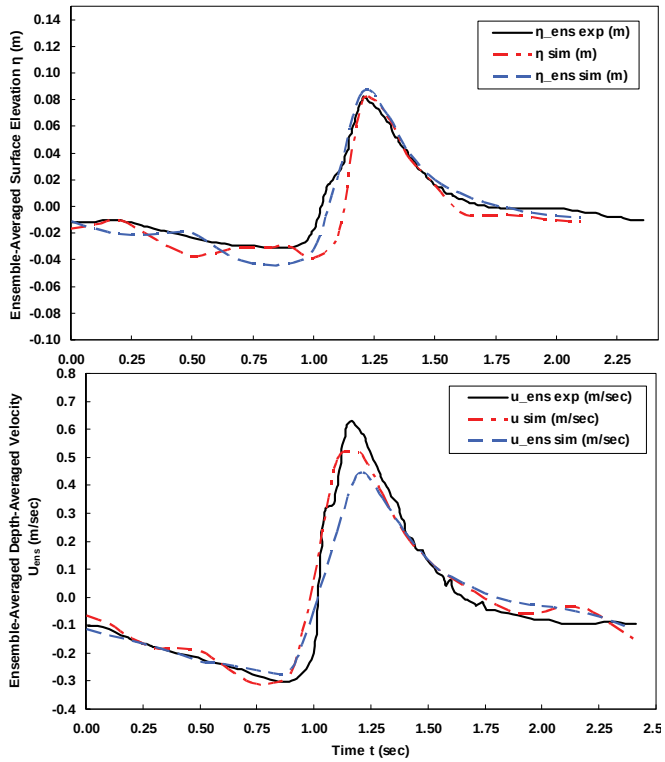

Fig. 6: Comparison of experimental (exp) against simulation (sim) data for ensemble-averaged (blue dashed line) and real-time (red dash-dotted line) raw values of free-surface elevation 'η' [upper graph] and depth-averaged velocities 'U' [lower graph] in the mid surf zone.

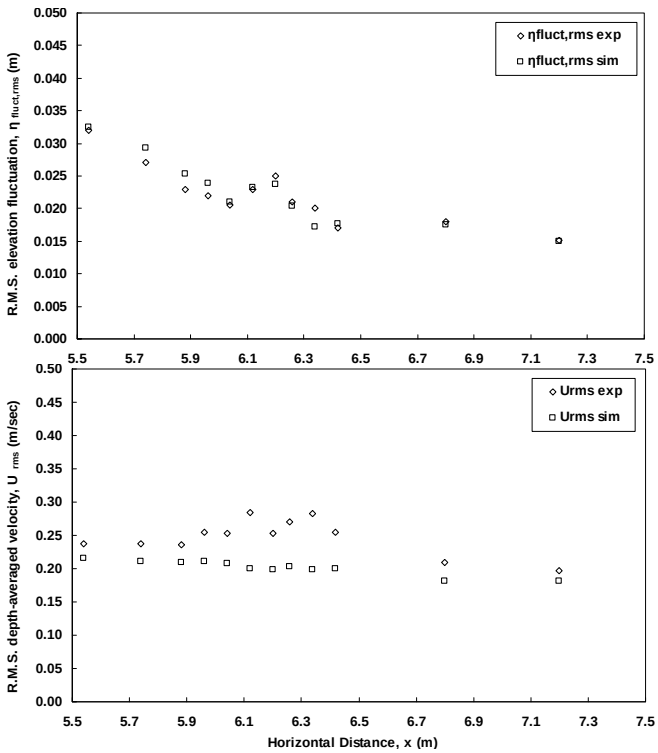

Fig. 7: Comparison of experimental (exp) and simulated (sim) rms values of free-surface elevation fluctuation '$\eta_{fluct,rms}$' [upper graph] and depth-averaged velocities '$\mathbf{U}_{rms}$' [lower graph].

In Fig. 6 relative values at a specific gauge in the advanced surf zone are presented together with indicative respective raw values. Following Makris et al. (2011) plausible agreement was pursued against SF05 data also in the mid surf zone for the refined resolution tests. At shear intensified regions, <**U**> was barely underestimated, probably due to lack of robust treatment for friction and boundary layer in SPH simulations or need for Δx values down to Kolmogorov length scales.

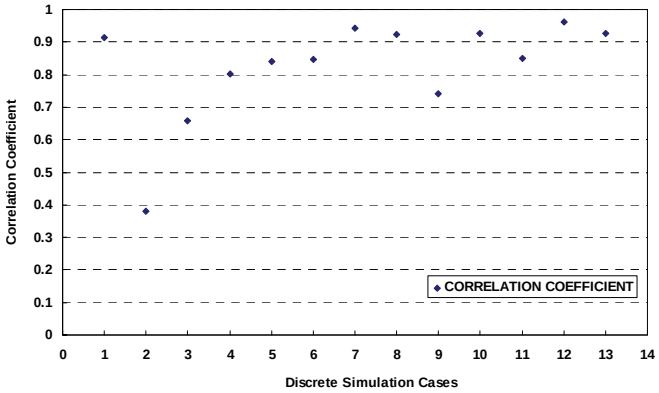

Fig. 8: Correlation coefficient of simulation vs. experimental $\eta_{fluct,rms}$.

In Fig. 7 the root mean square (rms) values of the fluctuating free-surface elevation, $\eta_{fluct}=<\eta>-\eta_{mean}$ (η_{mean} is period-averaged η) and **U** are given for test 12 along the surf zone. Comparisons against experimental data (Fig.7) and relevant Pearson correlation coefficients (Fig. 8) provided noticeable coincidence for $\eta_{fluct,rms}$ in refined resolution tests and somewhat debatable results for $\mathbf{U}_{rms}$ (correlation coefficient ~0.5). The latter applied mostly at the mid surf zone, where steep bore fronts were created and not at the outer and inner ones. However, SPHysics v.2 attributed apparently far better results than the RANS depth-integrated shallow water equations model used in SF05.

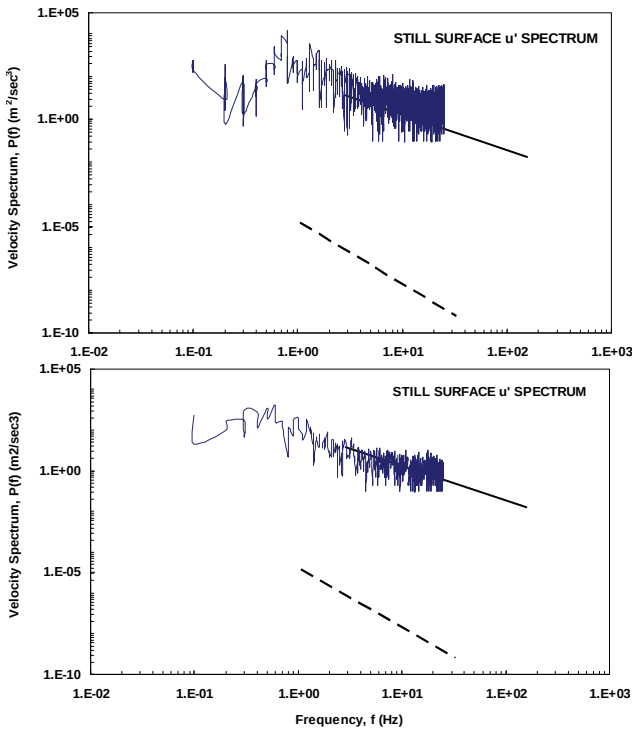

Fig. 9: Fourier spectra of simulated turbulent component of horizontal velocity **u**´ for the incipient breaking region and large recording time (test 6) [upper graph]. Same features for inner surf zone and fine spatial resolution (test 13) [lower graph]. Measurements at still surface level.

Turbulent Flow Features

An effort to describe several turbulent features, which are hard to obtain with the use of classic wave models, was pursued. Such features are the coherent turbulent structures, the recurring vorticity patterns and the power spectra of the turbulent (fluctuating) components of the Eulerian velocity field, $\mathbf{u}'=\mathbf{u}-\langle\mathbf{u}\rangle$, inside the surf and swash zones.

Velocity Fourier spectra. Fig. 9 shows the Fourier spectra of horizontal $\mathbf{u}'$ at still surface level, $P_{u'}(f)$ (f is frequency), derived by the velocity field of high recording time simulations (upper graph) and finest achieved resolution test (lower graph), at the incipient breaking region and inner surf zone respectively. A trend that followed the -5/3 gradient on the log/log scale, typical of isotropic (inertial sub-range) turbulence, was obvious up to a value of f=10Hz and somehow ongoing until the Nyquist filter limit of f=25Hz. Random turbulence below this frequency was lost in the averaging process. Improvement of our previous results (Makris et al., 2010b; 2011) was clear for high frequency bands, that correspond to either the SPS-treated scales or the smaller of the resolved large eddies. Higher than before spatial resolution and sufficient simulation cycles contribute positively to this upgrade in numerical results. The -3 gradient, typical of 2D frozen turbulence (Lessieur, 1990), was also sketched on the graphs (as in SF05), although it was never reproduced in any gauge and depth. SF05 report that turbulence quantities obtained were only superimposed residual values of relatively high f, not representative of all turbulence energy. Thus future rigorous analysis of Reynolds normal and shear stresses and turbulent kinetic energy will confirm if residual turbulence is close to or far from isotropic.

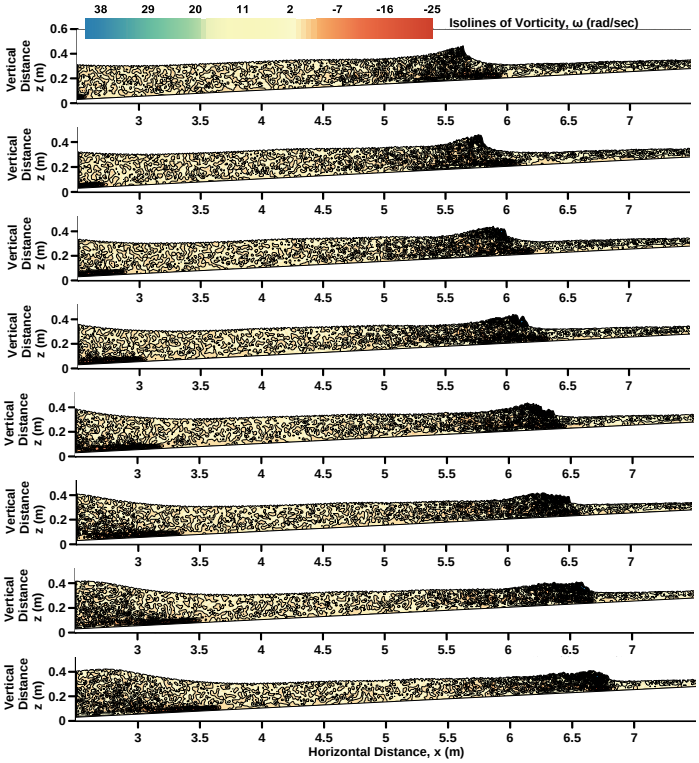

Fig. 10: SPHysics vorticity field under weak plunging breaking waves. Coherent turbulent structures and vortical patterns of large scale eddies.

Coherent turbulent structures. In Fig. 10 patterns of concentrated vorticity appearing periodically with the passage of the monochromatic waves are shown in a 2D cross-sectional plane. These are coherent turbulent structures involving from large-scale vortices down to small-scale eddies. Vorticity started to gain noticeable values at the toe of the surface roller as stated in Peregrine & Svendsen (1978). Hereupon concentrated vorticity spread in the whole surface roller region until the initiation of the breaking process. During the latter, confined multiple vortical structures became apparent. They were quickly permeated near and along the free surface as the turbulent bore was formed and stretched horizontally during its propagation just as reported in SF05. While the whole process was taking place, a thick layer of positive vorticity (clockwise rotating eddies) from the free surface to trough level was evident whereas a thin layer of negative vorticity (counter-rotative eddies) prevailed near the bed, just as in SF05 and Nadaoka et al, (1989). Flakes of negative vortical structures merged with positive ones and drifted apart in an inclined mode of about 45º following the principal axes of the mean strain rate of the phase-averaged velocity field around and behind the wave crest. This tilt almost coincides with the stretch direction of the obliquely descending eddies (Nadaoka et al. (1989) seaward of the plunging wave crest. 3D representation of the flow field will enlighten the matter and preliminary respective results seemed promising. The vorticity generation for test 4 is shown in the upper graphs (Fig. 10), where multiple coherent vortices originated and consequently spread out seaward relative to the crest before inclining towards the bed in the mid graphs. This might be considered to be the end of the plunging region and the start of bore propagation eventually resulting in the forming of two large coherent regions like the structures shown at the lower graphs. For the initial breakers, the maximum raw vorticity in our simulations was double compared to the mean vorticity (65 $\sec^{-1}$) in SF05 at the toe of the breaker. This quickly reduced to about the half later on and it was maintained for the bore propagation region, where the coherent vortices spread markedly along the surface just as in SF05. Everywhere else the flow was nearly irrotational except in the region upstream of the breaker, where there was observed torpid residual vorticity of low values from the passage of previous breakers (also shown in Fig. 1). The closer and bigger those whirls were, the more stretched became the flow field around saddle points between them giving rise to obliquely descending morphs, which faded and merged with the upcoming turbulent bore. Simultaneously, persisting largely elongated structures of negative vorticity were observed near the bed in front of the roller, initially similar to a mixing layer, just as in SF05 and Nadaoka et al. (1989). These and the formerly mentioned coherent structures in the roller region are most important in bed sediment pickup and suspension respectively, for they act as enclosed pockets that carry sediment with them, shaping its transport.

Mean vorticity vertical distributions. In Fig. 11 the vertical distributions of period-averaged vorticity ω_{mean} in the incipient breaking region for large (test 1) and small (test 13) Δx is presented. For high spatial resolution, concentrated small values of negative ω_{mean} were traced near the bed and an order of magnitude larger positive ω_{mean} appeared near the surface on a crooked line representing the projections of the aforementioned multiple coherent blocks on the gauge perpendicular line. For low particle resolution an exaggerated smooth vertical distribution of ω_{mean} reveals that vortical structures were not represented well at all. The SPS model became over-diffusive for these spatial scales by treating not only the small length scales of the turbulent flow but the large eddies too. Failure in wave height and velocities prediction, especially in shear intensified regions for low resolution simulations (Makris et al., 2009), upheld the former observation. In order for the SPS approach to work plausibly and let the SPH laminar approach to resolve the large eddies, even smaller Δx (involving millions of particles) should be tried in future studies.

Wave-induced mean flows (Undertow and Stokes drift)

Additionally we focused on the simulation of the wave-induced mean

flows in the surf zone, namely the cross-shore return-type flow called the undertow and the shoreward mass transport flow called the Stokes drift. In Fig. 12 the period-averaged kinematics for the surf zone (upper graph) and the whole computational domain (lower graph) were also obtained for test 12. The onshore current above trough level (Stokes drift) and the undertow below were clearly visible across the whole surf zone. Moreover, even the shoreward inversion of the mean flow, near the bed, was qualitatively well depicted. Please note that the velocity vector field was averaged over the 'wet' period (the time for which a point was immersed in water for a wave cycle) causing the occurrence of maximum values at the crest level exactly as in SF05. Averaging over the whole wave propagation and breaking event should reveal vertical distributions of mean flow velocities closing in on zero values at the crest envelope, like those suggested by Svendsen and Lorenz (1989). The maximum values for those distributions were traced during the initiation of breaking, whereas they gradually reduced in the bore region. Magnitudes decreased to really small values at and below the trough level, as the 'wet' period became equal to the 'real' wave period there. That was the reason for an obvious overall shoreward excess in momentum near the free surface, when we calculated the depth-averaged value of the mean velocity distribution. Naught balance should exist only if we had averaged over the whole wave propagation and breaking event. Another plausible attribute was the eloquent depiction of the propagating wave's advancing nonlinearity until it reached the breaking point (Fig. 12, lower graph). The wave setup level was well positioned compared to the crest and trough envelopes (Fig. 12). The upper graph representing the entire surf zone showed great similarities compared to the respective representation in SF05.

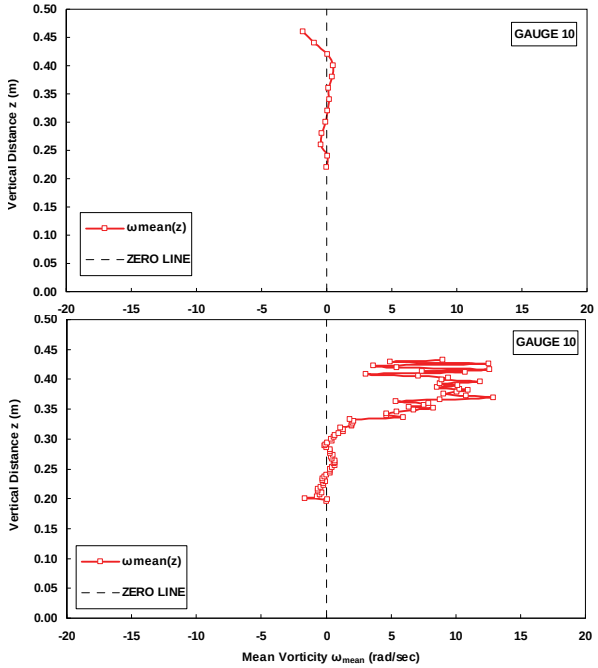

Fig. 11: Vertical distribution of time-averaged vorticity 'ω_{mean}' in the outer surf zone for low (upper) and high (lower graph) resolution.

Swash Zone Features

The onshore average run-up above the shoreline for the experimental data of SF05 was deduced from the mean elevation distribution at 24 gauges, through the use of a nonlinear polynomial trend. The derived value was found to be 0.595 m. Dimensionless ratios of simulated over experimental values of onshore run-up S_{ratio} for all discrete test cases were calculated and were presented in Fig. 13. The values near the 100% line are the most proper. This applied for Δx near the integral turbulence length scales. The rest of the tests incorporated either large heavy particles proving to reproduce spurious friction phenomena on the bottom boundary or small light particles with the opposite result. For the latter resolution, so small particles are assumed to resemble blobs reaching a terminal point up the solid slope, yet this should not be considered as actual run-up. Thus in general Δx equal or similar to the integral turbulence length scale should suffice for run-up calculations.

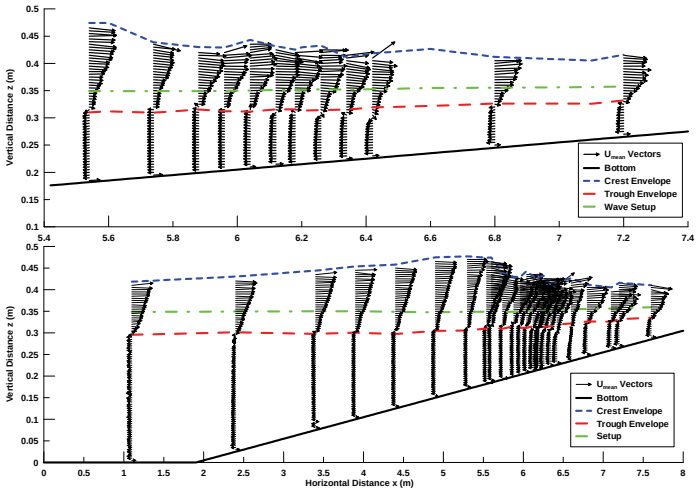

Fig. 12: 'Wet' time-averaged vertical distribution of velocity vectors at various gauges covering the entire surf zone [upper graph] and the whole computational field [lower graph]. Clear discrimination of the lower (undertow) and upper (Stokes drift) wave-induced mean flow regions, delimited by wave trough (red large dashed line), crest (blue small dashed line), and wave setup (green dash-dotted line) envelopes.

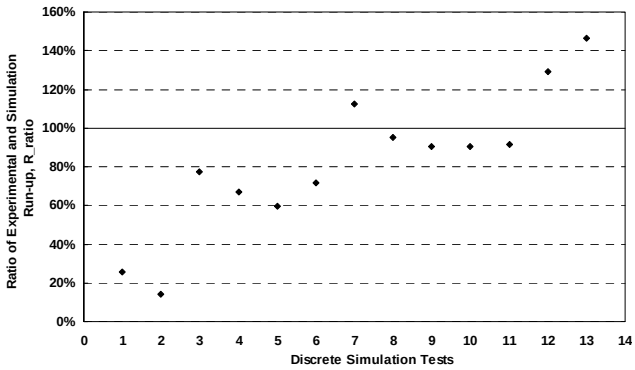

Fig. 13: Dimensionless ratios of simulated over experimental values of onshore run-up 'R' for discrete test cases.

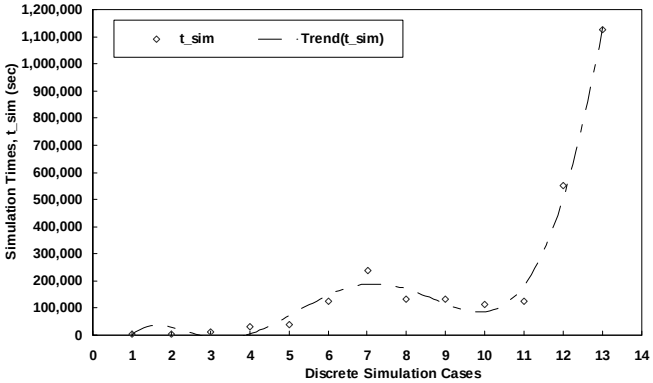

Fig. 14: Recorded simulation times 't_{sim}' for discrete test cases

Simulation Costs and Computer Attributes

Recorded times of discrete 'scalar' SPHysics code simulations (on Intel CPU i7-860 @2.8GHz, 4GB RAM) are presented in Fig. 14. It is more than obvious that increase of resolution led to exponential growth of the simulation time needed e.g. up to ~13.5 days for test 13. Based on the preceding Fourier spectral analysis, even finer spatial resolution should be implemented in order to get reasonable values of **u**´ and plausible distributions of $P_{u'}(f)$ for the whole water column and not only the free surface. This requirement puts forth the dire need for future use of new 'parallel' versions of SPHysics to run on GPUs (Hérault et al., 2010) or CPU clusters, in order to reduce simulation times especially for 3D simulations of real-life problems (millions of particles).

CONCLUSIONS

Refined resolution calibration of the most recent SPHysics v.2 model was attempted against the experimental data of Stansby and Feng (2005). The dynamics of near-shore nonlinear monochromatic waves breaking in weakly plunging form on a mild impermeable slope were investigated. Plausible agreement was achieved in terms of wave height distributions, wave setup, wave crest and trough envelopes, ensemble-averaged and rms values of free-surface elevation and depth-averaged velocities. Turbulent flow features inside the surf zone were also explored. Fourier spectra of turbulent components of velocities revealed isotropy in turbulence for rather high frequencies only in shear intensified regions such as the free surface in the incipient breaking point. Coherent turbulent structures and vorticity repetitive patterns were reproduced in a very satisfactory way as compared to respective experimental studies. Considerable amount of vorticity was generated at the front face of the breaking waves and then was entrained by large-scale eddies, into the underlying flow field, just as reported in Nadaoka et al., (1989). Vorticity appeared to be significant at the toe of the surface roller and gained magnitude at the steep front of the plunger as well as at the initial turbulent bore front, but reduced rapidly after, just as in Stansby and Feng (2005). Multiple coherent vortices seemed to disperse and leave an elongated layer of vorticity along the surface as the bore propagated. Coherent stuctures of anti-clockwise vorticity were also observed near the bed, below the bore region and in front of the pre-breaking surface roller, similarly to what was reported in relevant physical simulation attempts. Furthermore, the numerically derived period-averaged kinematics showed that the wave-induced mean flows (Stokes drift and undertow) were plausibly simulated, yielding rewarding results compared to Stansby and Feng (2005). Spatial resolution turned out to be the most significant factor in forming realistic results for SPS turbulence closure modeling combined with SPH similar to LES. Swash zone features were loosely discussed yet spatial discretization similar to the integral turbulence length scale seemed to suffice for run-up calculations. An effort to bend the extremely time-consuming computations, moving towards 1 to 2 million particles, with the use of a new 'parallel' version of the SPHysics code was set as a future research goal.

REFERENCES

Biausser, B, Grilli, ST, Fraunié, P (2003). "Numerical Simulations of Three-Dimensional Wave Breaking by Coupling of a VOF Method and a Boundary Element Method," *Proc 13th Int Offsh & Polar Eng Conf*, Honolulu, ISOPE, Vol 3, pp 333-339.

Bradford, SF (2000). "Numerical Simulation of Surf Zone Dynamics," *J Wtrway, Port, Coast and Ocean Eng*, Vol 126, No 1, pp 1-13.

Cox, DT, Kobayashi, N, and Okayasu, A (1994). "Vertical Variations of Fluid Velocities and Shear Stress in Surf Zones," *Proc 24th Intl Conf Coast Eng*, Kobe, ASCE, pp 98-112.

Dalrymple, RA, and Rogers, BD (2006). "Numerical Modeling of Water Waves with the SPH Method," *Coast Eng*, Vol 53, pp 141-147.

Gómez-Gesteira, M, Rogers, BD, Dalrymple, RA, Crespo, AJC, and Narayanaswamy, M (2010a). *User Guide for the SPHysics Code v2.0*.

Gómez-Gesteira, M, Rogers, BD, Dalrymple, RA, and Crespo, AJC (2010b). "State-of-the-art of Classical SPH for Free-Surface Flows," *J of Hydr Res*, Vol 48, Extra Issue, pp 6–27.

Grilli, ST, Guyenne, P, and Dias, F. (2001). "A Fully Non-Linear Model for Three-Dimensional Overturning Waves over an Arbitrary Bottom," *Int J Numer Meth Fluids*, Vol 35, pp 829-867.

Guyenne, P, and Grilli, ST (2003). "Computations of Three-Dimensional Overturning Waves in Shallow Water: Dynamics and Kinematics," *Proc 13th Int Offsh & Polar Eng Conf*, Honolulu, ISOPE, Vol 3, pp 347-352.

Hérault, A, Bilotta, G, Dalrymple, RA (2010). "SPH on GPU with CUDA," *J of Hyd Res*, Vol 48, Extra Issue, pp 74-79.

Iafrati, A (2009). "Numerical Study of the Effects of Breaking Intensity on Wave Breaking Flows," *J Fluid Mech*, Vol 622, pp 371-411.

Khayyer, A, Gotoh, H, and Shao, SD (2005). "Corrected Incompressible SPH Method for Accurate Water-Surface Tracking in Breaking Waves," *Coast Eng*, Vol 55, pp 236-250.

Lesieur, M (1990). *Turbulence in Fluids*, 2nd Ed, Kluwer.

Lubin, P, Glockner, S, Kimmoun, O, and Branger, H (2011). "Numerical Study of the Hydrodynamics of Regular Waves Breaking over a Sloping Beach," *Europ J of Mech - B/Fluids*, (accepted).

Makris, CV, Memos, CD, and Krestenitis, YN (2009). "Numerical Simulation of Near-Shore Wave Breaking Using SPH Method," *Proc 4th Int Short Conf on Applied Coast Res*, Barcelona, pp 241-252.

Makris, CV, Krestenitis, YN, and Memos, CD (2010a). "SPH Numerical Simulation of Surf Zone Characteristics," *Proc 6th Int Symp on Env Hydr*, Athens, Vol 1, pp 445-450.

Makris, CV, Krestenitis, YN, and Memos, CD (2010b). "SPHysics Code Validation Against a Near-shore Wave Breaking Experiment," *Proc 5th Int SPH Euro Res Intrst Com Workshop*, Manchester, pp 245-252.

Makris, CV, Memos, CD, and Krestenitis, YN (2011). "Modeling of Breaking Wave Dynamics, Surf Zone Turbulence and Wave-Induced Mean Flows with the SPH Numerical Method," *Proc 5th Int Short Conf on Applied Coast Res*, Aachen.

Monaghan, JJ (2005). "Smoothed Particle Hydrodynamics," *Rep Prog Phys*, Vol 68, pp 1703-1759.

Nadaoka, K, Hino, M, and Koyano, Y (1989). "Structure of the Turbulent Flow Field Under Breaking Waves in the Surf Zone," *J Fluid Mech*, 204, pp 359-387.

Peregrine, DH, and Svendsen, IA (1978). "Spilling Breakers, Bores and Hydraulic Jumps," *Proc 16th ICCE*, Hamburg, ASCE, pp 540-550.

Shao, S, and Ji, C (2006). "SPH Computation of Plunging Waves Using a 2-D Sub-Particle Scale (SPS) Turbulence Model," *Int J Numer Meth Fluids*, Vol 51, pp 913-936.

Stansby, PK, and Feng, T (2005). "Kinematics and Depth-Integrated Terms in Surf Zone Waves from Laboratory Measurement," *J Fluid Mech*, Vol 529, pp 279-310.

Stive, MJF (1984). "Energy Dissipation in Waves Breaking on Gentle Slopes," *Coast Eng*, Vol 8, pp 99-127.

Svendsen, IA, and Lorenz, RS (1989). "Velocities in Combined Undertow and Longshore Currents," *Coast Eng*, Vol 13, pp, 55-79.

Tian, Z, Perlin, M, and Choi, W (2010). "Energy Dissipation in Two-Dimensional Unsteady Plunging Breakers and an Eddy Viscosity Model," *J Fluid Mech*, Vol 655, pp 217-257.

Ting, FCK, and Kirby, JT (1994). "Observation of Undertow and Turbulence in a Laboratory Surf Zone," *Coast Eng*, Vol 24, pp 51-80.

Watanabe, Y, and Saeki, H (2002). "Velocity Field after Wave Breaking," *Int J Numer Meth Fluids*, Vol 39, pp 607-637.

Zhao, Q, Armfield, S, and Tanimoto, K (2004). "Numerical Simulation

of Breaking Waves by a Multi-Scale Turbulence Model," *Coast Eng*, Vol 51, pp 53-80.